

The phase space density of fermionic dark matter haloes

Shi Shao^{1*}, Liang Gao^{1,2}, Tom Theuns^{2,3}, and Carlos S. Frenk²

¹*The Partner Group of Max Planck Institute for Astrophysics, National Astronomical Observatories, Chinese Academy of Sciences, Beijing, 100012, China*

²*Institute of Computational Cosmology, Department of Physics, University of Durham, Science Laboratories, South Road, Durham DH1 3LE*

³*Department of Physics, University of Antwerp, Campus Groenenborger, Groenenborgerlaan 171, B-2020 Antwerp, Belgium*

26 September 2012

ABSTRACT

We have performed a series of numerical experiments to investigate how the primordial thermal velocities of fermionic dark matter particles affect the physical and phase space density profiles of the dark matter haloes into which they collect. The initial particle velocities induce central cores in both profiles, which can be understood in the framework of phase space density theory. We find that the maximum coarse-grained phase space density of the simulated haloes (computed in 6 dimensional phase space using the EnBid code) is very close to the theoretical fine-grained upper bound, while the pseudo phase space density, $Q \sim \rho/\sigma^3$, overestimates the maximum phase space density by up to an order of magnitude. The density in the inner regions of the simulated haloes is well described by a ‘pseudo-isothermal’ profile with a core. We have developed a simple model based on this profile which, given the observed surface brightness profile of a galaxy and its central velocity dispersion, accurately predicts its central phase space density. Applying this model to the dwarf spheroidal satellites of the Milky Way yields values close to 0.5 keV for the mass of a hypothetical thermal warm dark matter particle, assuming the satellite haloes have cores produced by warm dark matter free streaming. Such a small value is in conflict with the lower limit of 1.2 keV set by observations of the Lyman- α forest. Thus, if the Milky Way dwarf spheroidal satellites have cores, these are likely due to baryonic processes associated with the forming galaxy, perhaps of the kind proposed by Navarro, Eke and Frenk and seen in recent simulations of galaxy formation in the cold dark matter model.

Key words: methods: N-body simulations – methods: numerical –dark matter galaxies: haloes

1 INTRODUCTION

The standard cosmological model, the “ Λ cold dark matter model” (Λ CDM) has been tested over a huge range of scales, from the entire observable universe, probed by measurements of temperature anisotropies in the cosmic microwave background radiation (CMB; Komatsu et al. 2011), to the scales of galaxy clusters and individual bright galaxies, probed by large galaxy and Lyman- α forest surveys (Colless et al. 2005; Seljak et al. 2005; Zehavi et al. 2011). On smaller scales than this, there is no strong evidence to support the standard model. Yet, it is on such scales that the nature of the dark matter is most clearly manifest. In the standard model the dark matter consists of cold particles, such as the lightest stable particle predicted by Supersymmetry. There are, however, models of particle physics that predict lighter particles, such as sterile neutrinos, that would behave as warm (WDM), rather than cold dark matter (CDM) (see Feng 2010; Hooper 2012, for discussions of re-

cent experimental constraints). No current astronomical data can distinguish between these alternatives.

If the dark matter particles freeze out while in thermal equilibrium, their kinematics leave a predictable imprint in the power spectrum of primordial perturbations (Zel’dovich 1965). Hot dark matter particles, such as light neutrinos, decouple while still relativistic; their large thermal velocities dampen fluctuations below a ‘free streaming’ length, λ_{FS} , which is of the order of a few tens of megaparsecs at redshift $z = 0$ (Bond & Szalay 1983). Early N-body simulations showed that this is too large to be compatible with the level of clustering measured in the galaxy distribution (Frenk et al. 1983), thus ruling out light neutrinos as the dominant form of dark matter. Recent analyses of the power spectrum of the galaxy distribution (Cole et al. 2005), the Lyman- α forest (Viel et al. 2010) and the CMB (Komatsu et al. 2011) constrain the sum of the neutrino masses to be $\sum m_\nu < 0.58$ eV.

Cold dark matter particles decouple after they have become non-relativistic. For a typical cold, weakly interacting, massive particle, λ_{FS} is of the order of a parsec and the corresponding ‘Jeans’ mass is of the order of $10^{-6} M_\odot$ (Green et al. 2005); free streaming

* Email: shaoshi@bao.ac.cn

in this case is not relevant for galaxy formation. The intermediate case of warm dark matter corresponds to particles that decouple while still relativistic, yet become non-relativistic before the epoch of radiation-matter equality. Their free streaming scale could then be of order the size of a galaxy, in which case they can affect the build-up of dark matter haloes and of the galaxies forming within them (Bode et al. 2001; Lovell et al. 2012), as well as the formation of the first stars (Gao & Theuns 2007). Dark matter particles need not freeze out in thermal equilibrium, as is the case, for example, of the axion and the sterile neutrino discussed by Boyarsky et al. (2009a). In this case, the relation between the dark matter particle mass and λ_{FS} is more complex. Boyarsky et al. (2009b) discuss current limits on such WDM models.

Except perhaps in the central regions of galaxies, the dynamics of dark matter particles are driven purely by their own gravity and are thus governed by the Vlasov-Poisson equations. Then, according to Liouville's theorem, the distribution function, $f(\mathbf{x}, \mathbf{v}, t)$, of the particles – the mass per unit volume in phase space – is time-independent, $Df(\mathbf{x}, \mathbf{v}, t)/Dt = 0$. Phase space mixing, or coarse-graining, can only decrease the phase space density below this fine-grain bound set by the nature of the particles. Tremaine & Gunn (1979) used this property to constrain the nature of stable leptons as the dominant form of dark matter. Since the intrinsic velocities of CDM particles are small, their fine-grained phase space density limit is very high and such haloes are cuspy (e.g. Navarro et al. 1996, 1997; Diemand et al. 2008; Stadel et al. 2009; Navarro et al. 2010; Gao et al. 2012). For WDM (and *a fortiori* for HDM), the phase space density bound is much lower and such haloes develop central cores (Hogan & Dalcanton 2000; Bode et al. 2001).

Evidence for central cores in galaxies is controversial (see Frenk & White 2012, and references therein for a recent discussion). Recently, Walker & Peñarrubia (2012) have argued that the kinematics of the Fornax and Sculptor dwarf spheroidals in the Milky Way rule out central density cusps, but Strigari et al. (2010a) have shown that the data for these and other dwarfs are consistent with the cuspy profiles seen in cold dark matter simulations. On the other hand, Boylan-Kolchin et al. (2011), Lovell et al. (2012) and Parry et al. (2012) have shown that the central concentration of the dark matter haloes of nine dwarf spheroidals are lower than expected in simulations of cold dark matter haloes (Springel et al. 2008) (but see Wang et al. (2012)). Although baryonic processes associated with the forming galaxy could lower the central density of haloes and even induce a core (Navarro et al. 1996; Read & Gilmore 2005; Mashchenko et al. 2008; Pontzen & Governato 2012), it is also possible, in principle, that the kind of phase space constraints just discussed could be at work at the centres of the dwarf spheroidals.

In this paper we investigate the effect of primordial dark matter particle thermal velocities on halo density profiles. To this aim, we carry out N-body simulations from initial conditions in which the power spectrum has a small-scale cut-off and the particles representing the dark matter have significant thermal velocities. Our setup does not correspond exactly to any particular HDM or WDM particle candidate. Rather, we are interested in the more general problem of how phase space constraints are satisfied in cosmological N-body simulations. In particular, we determine the level at which the Tremaine & Gunn (1979) bound is satisfied. We then model our numerical results, generalise them to the case of specific WDM candidates, and apply them to Milky Way satellites.

As we were completing this work, Macciò et al. (2012) posted a paper on Arxiv investigating similar issues to those of interest here, using similar numerical techniques. However, a numerical er-

ror in their initial conditions¹ requires a re-interpretation of their results.

The remainder of this paper is structured as follows. In Section 2, we describe our set of numerical simulations. In Section 3, we briefly review relevant aspects of phase space theory and describe our methods for calculating the coarse-grained phase space density in the simulations. In Section 4, we investigate phase and real space density profiles of dark matter haloes and compare these with our theoretical estimates. In Section 5, we use a model based on our numerical simulations to revise the lower mass limit of WDM particles. Our paper concludes in Section 6 with a summary and discussion.

2 PHASE SPACE DENSITY

In this section, we briefly review those aspects of phase space density theory that are relevant to general fermionic dark matter particles.

2.1 Fine-grained phase space density

The evolution of a system of collisionless particles is described by the Vlasov equation. According to Liouville's theorem, the fine-grained phase space density, $f(\mathbf{x}, \mathbf{v}, t)$ – the mass density in an infinitesimal six-dimensional phase space volume, $d^3\mathbf{x}d^3\mathbf{v}$, centred on the point (\mathbf{x}, \mathbf{v}) at time t – is conserved: $Df/Dt = 0$ (see e.g. Peebles & Yu (1970) for the General Relativistic description).

Following Tremaine & Gunn (1979), Madsen (1991) and Hogan & Dalcanton (2000), using the Fermi-Dirac occupation distribution we can derive an upper limit on \mathcal{F}_{FD} , the fine-grained phase space density of a relativistic fermionic relic in kinetic equilibrium:

$$\begin{aligned} \mathcal{F}_{\text{FD}}(\mathbf{p}) &= \frac{g}{(2\pi\hbar)^3} \frac{1}{e^{(E-\mu)/(k_{\text{B}}T)} + 1} \\ &\leq \frac{g}{2(2\pi\hbar)^3}. \end{aligned} \quad (1)$$

Here, $E = [(mc^2)^2 + (pc)^2]^{1/2}$ is the energy of a particle with mass m and momentum \mathbf{p} , and the chemical potential, $\mu = 0$ for thermal relics; g is the number of degrees of freedom (Kolb & Turner 1990). This expression may be more familiar from the derivation of the equation of state of degenerate fermions. Warm dark matter particles are relativistic when they decouple, *i.e.* when $T = T_D$, the decoupling temperature. After decoupling both the energy and the temperature decline in proportion to $(1+z)$ and hence the shape of the Fermi-Dirac distribution remains unchanged. Finally, under a Lorentz transformation, lengths contract in proportion to the Lorentz factor, γ , whereas momenta increase in proportion to $1/\gamma$ so the phase space density is an invariant.

The function \mathcal{F}_{FD} is the number density of particles per unit volume in momentum space, an appropriate choice when the particles are relativistic. When the particles become non-relativistic, we can write the phase space density, f_{FD} , in terms of the *mass* density of particles per unit volume in *velocity* space, which introduces

¹ The velocity dispersion of the dark matter particles in the initial conditions of Macciò et al. (2012) is a factor of $\sqrt{3}$ larger than assumed.

a factor m^4 , so the non-relativistic version of Eqn. (1) becomes

$$\begin{aligned} f_{\text{FD}}^{\text{max}} &= \frac{g m^4}{2(2\pi\hbar)^3} \\ &= 0.42 M_\odot \text{ kpc}^{-3} (\text{km s}^{-1})^{-3} \frac{g}{2} \left(\frac{m c^2}{0.03 \text{ keV}} \right)^4. \end{aligned} \quad (2)$$

In the linear regime, the density of these non-relativistic particles decays as $(1+z)^3$ but their peculiar velocities decay as $(1+z)$; hence this bound does not evolve with redshift, as expected.

2.2 Coarse-grained phase space density

The coarse-grained phase space density, $F(\mathbf{x}, \mathbf{v}, t)$, is defined as the mass density in a *finite* six-dimensional phase space volume, $\Delta^3 \mathbf{x} \Delta^3 \mathbf{v}$, centered on the point (\mathbf{x}, \mathbf{v}) at time t . The averaging process decreases the phase space density and hence $F \leq f$ (see, for example, Tremaine et al. (1986) and Mathur (1988) for the application of Liouville's theorem in an astronomical setting). Phase mixing is expected to be small in the region with the highest phase space density, and the maximum value of F for a system is therefore expected to be close to the value of f (Lynden-Bell 1967). Of course, in any real system, baryonic effects may increase or decrease the phase space density. In a simulated dark matter halo we can estimate F in 6 dimensions and verify whether indeed $F^{\text{max}} \leq f_{\text{FD}}^{\text{max}}$; we will do so below.

We begin by discussing various ways in which F can be estimated for a dark matter halo. We assume the central part of the halo to have a pseudo-isothermal density profile (e.g. Kent 1986; Begeman et al. 1991), which is a good fit to the simulated dark matter halo discussed below. This profile is given by

$$\rho(r) = \frac{\rho_0}{1 + (r/r_c)^2}, \quad (3)$$

where ρ_0 is the core density and r_c the core radius. The corresponding asymptotically flat circular velocity is $V_c = (4\pi G \rho_0 r_c^2)^{1/2}$. Assuming isotropic orbits V_c is related to the one-dimensional velocity dispersion σ , by $V_c = \sqrt{2}\sigma$. Under these assumptions, central density, core radius and velocity dispersion are related by

$$\rho_0 = \frac{1}{2\pi G} \frac{\sigma^2}{r_c^2}. \quad (4)$$

To obtain the corresponding coarse-grained phase space density, we need to know the velocity distribution function. Dynamically relaxed systems often have a Maxwellian velocity distribution, and we will assume this to be a good description for the central regions of the dark matter halo (Vogelsberger et al. 2009). The maximum density in velocity space is then $(2\pi\sigma^2)^{-3/2}$, and therefore the maximum coarse-grained phase space density, which occurs at the centre of the halo, is

$$\begin{aligned} F_{\text{iso}}^{\text{max}} &= \frac{\rho_0}{(2\pi\sigma^2)^{3/2}} \\ &= \frac{1}{(2\pi)^{5/2} G} \frac{1}{\sigma r_c^2} \end{aligned} \quad (5)$$

$$\begin{aligned} &= 0.06 M_\odot \text{ kpc}^{-3} (\text{km s}^{-1})^{-3} \\ &\times \left(\frac{\sigma}{100 \text{ km s}^{-1}} \right)^{-1} \left(\frac{r_c}{20 \text{ kpc}} \right)^{-2}. \end{aligned} \quad (6)$$

If the core is due to free-streaming of a WDM particle, then requiring $F_{\text{iso}}^{\text{max}} \leq f_{\text{FD}}^{\text{max}}$ constrains the WDM particle mass to be

$$m c^2 \left(\frac{g}{2} \right)^{1/4} \geq 8.2 \text{ keV} \left(\frac{\sigma}{\text{km s}^{-1}} \right)^{-1/4} \left(\frac{r_c}{\text{pc}} \right)^{-1/2}. \quad (7)$$

To derive the limit in Eqn. (5) we had to make an assumption about the form of the density profile of the central halo. Boyarsky et al. (2009a) introduced a ‘coarsest’ phase space density, $F_{\text{Boy}}^{\text{max}}$, which corresponds to a maximal coarse graining and does not require this assumption. Instead it makes use of the value of the enclosed mass, $M(R)$, of the halo over the whole available phase space volume $\Delta \mathbf{x} \Delta \mathbf{v} = (4\pi/3)^2 R^3 v_\infty^3$, where v_∞ is the local escape speed. For isotropic orbits, $v_\infty \geq \sqrt{6}\sigma$, leading to the maximum coarse-grained value of F of

$$F_{\text{Boy}}^{\text{max}} = \frac{\rho_0}{8\pi\sqrt{6}\sigma^3} \approx \frac{3 \ln 2}{16\sqrt{6}\pi^2 G} \frac{1}{\sigma r_h^2} \approx 0.18 F_{\text{iso}}^{\text{max}}, \quad (8)$$

where r_h is the half-light radius, defined by Pryor & Kormendy (1990),

$$\rho_0 = \frac{3 \ln 2}{2\pi G} \frac{\sigma^2}{r_h^2}. \quad (9)$$

This calculation is less restrictive and hence $F_{\text{Boy}}^{\text{max}} < F_{\text{iso}}^{\text{max}}$, as should be.

Finally, an often used *approximation* to F is

$$Q \equiv \frac{\rho}{\langle v^2 \rangle^{3/2}}, \quad (10)$$

introduced by Hogan & Dalcanton (2000) and more recently used, for example, by Taylor & Navarro (2001); Ascasibar et al. (2004); Dehnen & McLaughlin (2005); Peirani et al. (2006); Hoffman et al. (2007); Colín et al. (2008); Vass et al. (2009); Navarro et al. (2010). We will refer to this as a *pseudo* phase space density, since it only has the dimensions of F , but it is not a proper coarse-grained average of f . Indeed, the maximum value of Q for the halo profile of Eqn. (3) under the assumptions of isotropic Maxwellian velocities, is

$$Q^{\text{max}} = \frac{(2\pi)^{3/2}}{3\sqrt{3}} F_{\text{iso}}^{\text{max}} \approx 3.03 F_{\text{iso}}^{\text{max}}. \quad (11)$$

The upper bound to the fine-grained distribution for thermal fermions discussed by Hogan & Dalcanton (2000) is very similar to the value in Eqn.(2) above, $f_{\text{Hogan}}^{\text{max}} \approx 0.97 f_{\text{FD}}^{\text{max}}$ (see also Boyarsky et al. (2009a)). Requiring $Q^{\text{max}} \leq f_{\text{Hogan}}^{\text{max}}$ then overestimates the constraint on the dark matter particle mass by a factor of $(3.12)^{1/4}$.

2.3 Coarse-grained phase space density in simulations

A robust measurement of F in an N -body system requires a full six-dimensional calculation. In recent years, a number of independent approaches have been developed that allow such a calculation (Arad et al. 2004; Ascasibar & Binney 2005; Sharma & Steinmetz 2006; Vogelsberger et al. 2008). The method of Arad et al. (2004) uses the Delaunay tessellation of the N particles in 6 dimensional (\mathbf{x}, \mathbf{v}) phase space. Two other algorithms, Fi-EstAS (Ascasibar & Binney 2005) and EnBiD (Sharma & Steinmetz 2006), are based upon the idea of a binary $k-d$ -tree, *i.e.* repeated subdivisions of phase space in each of its 6 dimensions into nodes that contain (approximately) the same number of particles until each node contains a single particle. Both the Delaunay tessellation and the $k-d$ tree then associate a ‘volume,’ V_i , to a particle, and the corresponding phase space density is simply m_{particle}/V_i , where m_{particle} is the mass of the particle in the simulation. These algorithms contain adjustable parameters that can be chosen to improve the estimates. For example, Ascasibar & Binney (2005) include a

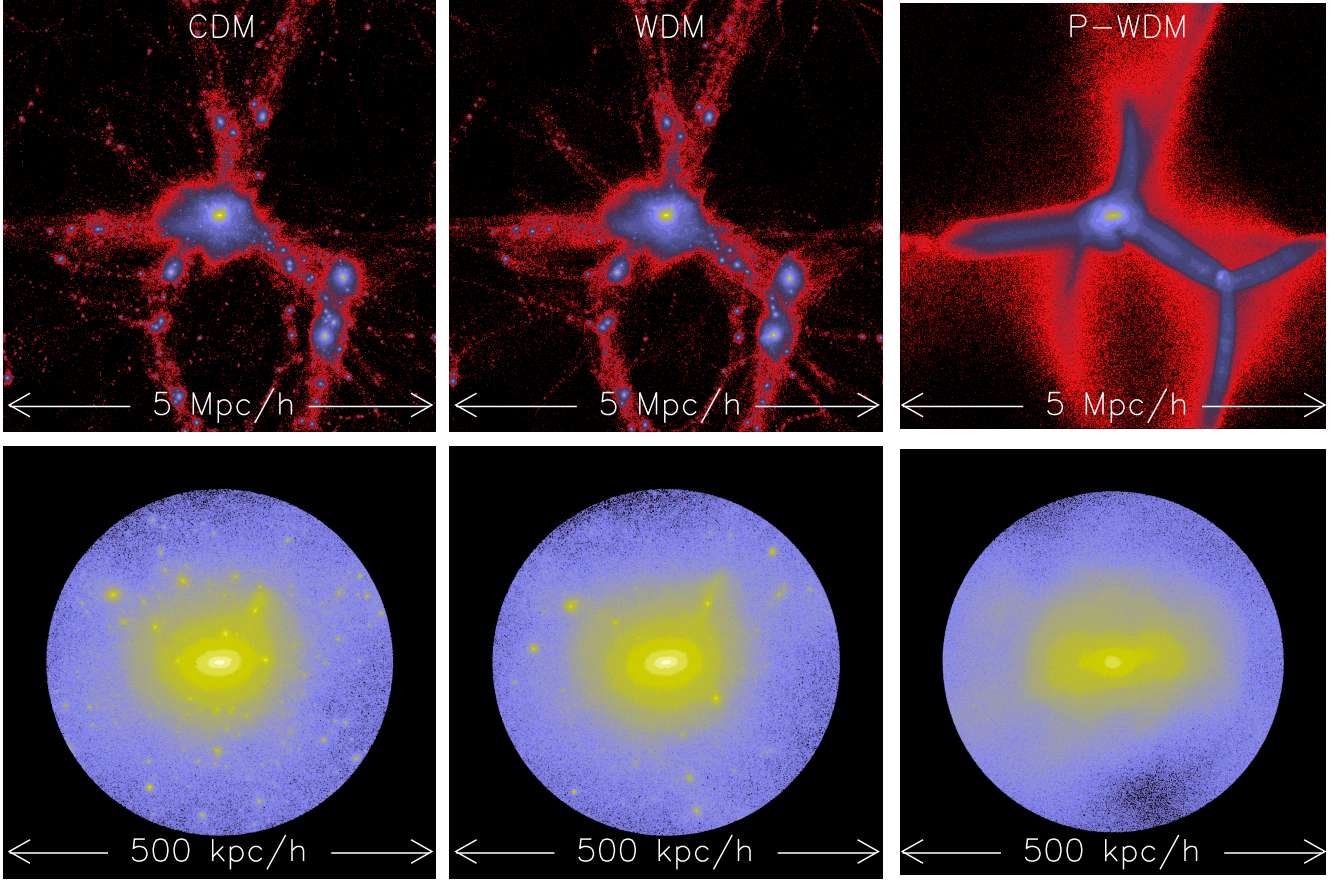


Figure 1. Projected density in a $5h^{-1}\text{Mpc}$ cube at $z = 0$ for the CDM, WDM, and P-WDM simulations (left to right). The top panels show the full simulation volume in a slice of $1.5h^{-1}\text{Mpc}$; the bottom panels zoom in on the most massive halo. As expected, features on scales larger than the free-streaming length are very similar, but on smaller scales the WDM runs have much less substructure. Model P-WMD, which had substantial initial random velocities, has almost no substructure at all.

boundary correction to improve the behaviour of the method at low density and smoothing kernels to reduce particle noise.

In this paper we make use of the publicly available EnBiD code (Sharma & Steinmetz 2006) to estimate the coarse-grained phase space density in our simulations. EnBiD employs a *Shannon Entropy* formulation which gives accurate results in high density regions. We have included the ‘boundary correction’ but did not use the smoothing option because it may underestimate the highest phase space density in a dark matter halo, which is crucial in this study. We will denote the coarse-grained phase space density of the simulated haloes calculated using EnBiD as F_{NB}

3 N-BODY SIMULATIONS

3.1 Physical requirements

If dark matter particles have large intrinsic velocities at early times, two distinct physical effects become important: free streaming out of density perturbations and a maximum achievable phase space density. In the linear regime, the WDM power spectrum of fluctuations, $P_{\text{WDM}}(k)$, is suppressed relative to the CDM power spectrum, $P_{\text{CDM}}(k)$, by a factor

$$T^2(k) \equiv \frac{P_{\text{WDM}}(k)}{P_{\text{CDM}}(k)}, \quad (12)$$

where k is the wavevector. Free streaming introduces a smallest wavevector, k_{H} , for which $T < 1$, and some authors refer to $2\pi/k_{\text{H}}$ as the ‘free-streaming length’. However, when considering structure formation, it is more useful to characterise the effects of free streaming by the value of $k_{\text{FS}} = 2\pi/\lambda_{\text{FS}}$ for which the amplitude of the power spectrum is reduced by a factor two relative to the CDM case, such that $T^2(k = k_{\text{FS}}) = 1/2$. The shape of the function $T(k)$ depends on the nature of the dark matter. A commonly used approximation for thermally produced WDM particles is

$$T(k) = (1 + (\alpha k)^2)^{-5}, \quad (13)$$

(Bode et al. 2001). For this case,

$$\lambda_{\text{FS}} = 23.45 \alpha,$$

$$\alpha = 0.05 \left(\frac{\Omega_{\text{WDM}}}{0.3} \right)^{0.15} \left(\frac{h}{0.72} \right)^{1.3} \left(\frac{mc^2}{\text{keV}} \right)^{-1.15} h^{-1} \text{Mpc}, \quad (14)$$

where Ω_{WDM} is the total WDM density today in units of the critical density, m is the WDM particle mass, and $H = 100 h \text{ km s}^{-1} \text{ Mpc}^{-1}$ is the Hubble constant at $z = 0$ (Bode et al. 2001). The numerical coefficient depends on the effective number of degrees of freedom, g_X , of the particle and we have assumed $g_X = 1.5$. With this definition we find

$$\lambda_{\text{FS}} = 1.2 \left(\frac{\Omega_{\text{WDM}}}{0.3} \right)^{0.15} \left(\frac{h}{0.72} \right)^{1.3} \left(\frac{mc^2}{\text{keV}} \right)^{-1.15} h^{-1} \text{Mpc}; \quad (15)$$

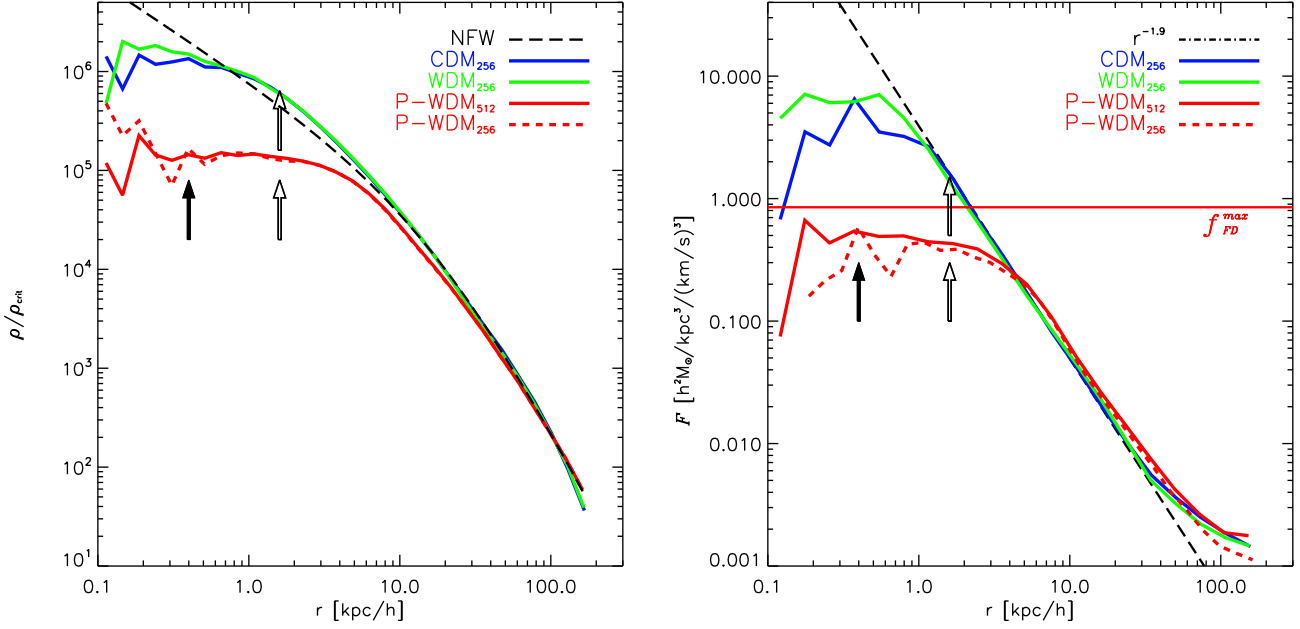


Figure 2. Mean, radially averaged density profile, $\rho(r)$ (left), and coarse-grained phase space density profile, $F_{\text{NB}}(r)$ (right), for the most massive halo in the CDM (blue), WDM (green) and P-WDM (red) simulations. Phase space densities were computed using the EnBiD code. The black-dashed lines are NFW and power-law fits to ρ and F_{NB} respectively for the CDM model. Different line styles correspond to simulations of different numerical resolution, as given in the legend, with arrows indicating twice the corresponding softening lengths. The CDM and WDM profiles are nearly indistinguishable, with $\rho(r)$ and $F_{\text{NB}}(r)$ well fit by the NFW and power-law profiles respectively. In contrast, the P-WDM model, which has significant initial thermal velocities, develops a core. The maximum value of the phase space density, F_{NB} , in the P-WDM model is close to, but smaller than the fine-grained upper limit, $f_{\text{FD}}^{\text{iso}}$, indicated by the horizontal red line.

the corresponding mass is

$$\begin{aligned} M_{\text{FS}} &\equiv \frac{4\pi}{3} \rho_m \lambda_{\text{FS}}^3 \\ &= 6 \times 10^{11} \left(\frac{\Omega_{\text{WDM}}}{0.3} \right)^{1.45} \left(\frac{h}{0.72} \right)^{3.9} \left(\frac{mc^2}{\text{keV}} \right)^{-3.45} h^{-1} M_{\odot}. \end{aligned} \quad (16)$$

We will refer to λ_{FS} as the free-streaming scale²

The second important effect is the limit on the phase space density achievable by dark matter particles with significant primordial thermal velocities. This induces a core radius, r_c , in collapsed haloes which, for thermal dark matter relics, scales with the velocity dispersion of the halo, σ , as $r_c \propto \sigma^{-1/2} m^{-2}$ (Hogan & Dalcanton 2000; Bode et al. 2001). Free streaming prevents haloes of virial radius³ $R_{200} \lesssim \lambda_{\text{FS}}$ from forming in significant numbers. As we will show below, the core radius of such haloes is $r_c \ll \lambda_{\text{FS}}$. Since $r_c \propto \sigma^{-1/2}$, the ratio r_c/R_{200} is even smaller for more massive haloes.

The small value of the ratio r_c/R_{200} makes it challenging to investigate core radii in simulations since the calculation needs to resolve the huge dynamic range between r_c and λ_{FS} . This is not currently practical for values of λ_{FS} typical of those expected in WDM models. However, if one is interested in the more general

problem of the relationship between r_c and the phase space density, it is not necessary for the cut-off in the power spectrum to correspond to the thermal velocities of a particular dark matter candidate. This is the approach we take in this study: we perform a numerical experiment by choosing a value of λ_{FS} but giving the particles much larger intrinsic velocities than would be appropriate for a WDM particle of mass m according to Eqn. (14). For brevity, we will refer to these models as pseudo-WDM models (P-WDM). We stress that this is not a self-consistent dark matter model: the resulting core radii will be much larger than expected for a WDM particle of that mass, but this is immaterial for our purposes. This procedure is similar to that adopted by Macciò et al. (2012). For comparison, we also investigate a self-consistent WDM model in which the initial thermal velocities are compatible with the cut-off in the power spectrum. Since the thermal velocities are now much smaller than the initial linear gravitational velocities, we expect their effect to be negligible.

3.2 Simulation details

All our simulations are of periodic cubic volumes of linear size $5h^{-1}$ Mpc. The assumed cosmological parameters are $(\Omega_m, \Omega_\Lambda, h, \sigma_8) = (0.3, 0.7, 0.7, 0.9)$, but the exact choice of these numbers is not important here. We have run two reference simulations: a standard Λ CDM (labelled CDM) and a self-consistent Λ WDM (labelled WDM) model. These have 256^3 particles, corresponding to an N -body particle mass of $6.2 \times 10^5 h^{-1} M_{\odot}$. The CDM transfer function was computed using

² Unfortunately, not all authors agree on a single definition of λ_{FS} .

³ We define the virial radius, R_{200} , of a cosmological dark matter halo as the radius within which the mean density is 200 times the critical density. The corresponding enclosed mass is M_{200} .

Table 1. Simulation details. In all cases the assumed cosmological parameters are $(\Omega_m, \Omega_\Lambda, h, \sigma_8) = (0.3, 0.7, 0.7, 0.9)$ and the simulation cube is $5h^{-1}$ Mpc on a side. The WDM and pseudo-WDM (P-WDM) models use the CDM power spectrum suppressed by $T^2(k)$ from Eqn. (13), using the parameters for a thermal WDM particle of mass $mc^2 = 2$ keV with $g = 2$ spin degrees of freedom. The corresponding free-streaming length is $\lambda_{\text{FS}} \approx 0.5 h^{-1}$ Mpc. The added velocities for the WDM model are consistent with the WDM particle properties, whereas for the P-WDM run, they correspond to those of an $mc^2 = 0.03$ keV thermal WDM particle.

Name	Number of particles	particle mass M_\odot	softening ϵ kpc
CDM	256^3	6.2×10^5	0.8
WDM	256^3	6.2×10^5	0.8
P-WDM ₂₅₆	256^3	6.2×10^5	0.8
P-WDM ₅₁₂	512^3	7.8×10^4	0.2

CMBfast (Seljak & Zaldarriaga 1996). For the WDM simulation, the power spectrum of the initial conditions was obtained by multiplying the CDM spectrum by $T(k)^2$, as given by Eqn. (13). The assumed free streaming length scale, $\lambda_{\text{FS}} \approx 0.5 h^{-1}$ Mpc, corresponds to a 2 keV thermal relic WDM particle and each particle is given the appropriate random velocity drawn from a Fermi-Dirac distribution. For definiteness we will always assume the WDM particle has $g = 2$ spin degrees of freedom.

The pseudo-WDM simulations (labelled P-WDM) have a similar set up to the WDM case, except that the random velocities are much larger and would correspond to those appropriate to a WDM particle of mass 0.03 keV. For ease of comparison, the Gaussian random field used to initialise the simulations uses the same phases for all three models. To enable statistical comparisons, we carried out a further 3 P-WDM simulations using the same cosmological parameters but different realisations of the initial conditions; these are denoted P-WDM₂₅₆. Finally, to investigate numerical convergence we carried out one simulation with 8 times better mass resolution, also with several different realisations of the initial conditions. These are denoted by P-WDM₅₁₂. The starting redshift for the CDM and WDM run was $z = 100$, but for the P-WDM runs it was $z = 20$ since in this case structure formation is significantly delayed compared to the CDM case. Table 1 summarises the parameters of the simulations. All our simulations were performed with the GADGET-3 code, an improved version of GADGET-2 (Springel 2005).

3.3 Comparisons of CDM and WDM simulations

Images of the CDM, WDM and P-WDM₂₅₆ simulations are displayed in Fig. 1 for the fiducial 256^3 particle run. As anticipated, the overall appearance of the main halo in the three simulations is very similar, but the amount of small-scale substructure is very different. The cut-off in the initial power spectrum in the WDM simulations has the effect of suppressing the formation of structure on scales below λ_{FS} . This is the reason why there are far fewer substructures in the WDM than in the CDM images. The large initial random velocities in the P-WDM case further smooths out the mass distribution, suppressing the formation of structures with velocity dispersion smaller than the amplitude of the random velocities.

The structure of the most massive halo in the CDM model, and the corresponding haloes in WDM and P-WDM, are compared in more detail in Fig. 2. These haloes all have fairly similar total mass, $M_{200} \sim 1.5 \times 10^{12} h^{-1} M_\odot$ for both CDM and WDM,

and $M_{200} \sim 1.0 \times 10^{12} h^{-1} M_\odot$ for P-WDM₅₁₂. The density profiles of the CDM and WDM runs are nearly indistinguishable from each other, demonstrating that for this self-consistent WDM model neither free streaming nor the (relatively small) initial intrinsic velocities affect the overall structure of the halo. For this choice of WDM parameters this is expected and has been seen in previous work (e.g. Bode et al. 2001; Colín et al. 2008). In contrast, the P-WDM₂₅₆ model, with its significantly larger intrinsic velocities, does form a core. Comparison of models P-WDM₂₅₆ and the eight times higher resolution P-WDM₅₁₂ shows that the core is numerically well resolved and converged.

The phase space density profiles of models CDM and WDM are also virtually indistinguishable; they are consistent with a power law, as found in previous studies (Fig. 2, right panel). Once again, neither free streaming nor intrinsic velocities affect the profile. On the other hand, in the P-WDM models a well-resolved core in the phase space profile develops. The coarse-grained phase space density, F_{NB} , computed using EnBiD, has a maximum of $F_{\text{NB}}^{\text{max}} \sim 0.5 h^2 M_\odot \text{ kpc}^{-3} (\text{km s}^{-1})^{-3}$, close to but smaller than the value of $f_{\text{FD}}^{\text{max}} = 0.85 h^2 M_\odot \text{ kpc}^{-3} (\text{km s}^{-1})^{-3}$ (shown as the horizontal red line) calculated from Eqn.(2) for a WDM particle of mass $mc^2 = 0.03$ keV. This demonstrates that our simulation methods and our calculation of phase space densities using EnBiD are sufficiently accurate to follow correctly the formation of cores due to the WDM intrinsic velocities. Given the good numerical convergence of the profiles, we use our three P-WDM₂₅₆ simulations with different initial random phases to obtain statistical results in more detail below.

In contrast, the fine-grained phase space density bound for the standard 2keV thermal relic is $f_{\text{FD}}^{\text{max}}(mc^2 = 2\text{keV}) = 1.7 \times 10^7 h^2 M_\odot \text{ kpc}^{-3} (\text{km s}^{-1})^{-3}$, ~ 7 orders of magnitude larger than for the P-WDM case. The corresponding size of the core is nearly two orders of magnitude smaller, and is well within the smoothing length of our simulations. Clearly, as we had anticipated, these simulations are not able to resolve the core of the WDM model.

3.4 Physical and phase space density profiles

As we have shown in Fig. 2, the most massive halo in the P-WDM simulations develops a central, near uniform density core of radius a few kiloparsecs. This behaviour is very different from the cuspy, $\rho(r) \propto 1/r$, profiles familiar from CDM simulations (Navarro et al. 1996, 1997, hereafter NFW). Fig. 3 shows density profiles for a further 9 numerically well-resolved haloes from the series of P-WDM runs, with masses ranging from $2.1 \times 10^{11} h^{-1} M_\odot$ to $1.5 \times 10^{12} h^{-1} M_\odot$. All nine haloes exhibit well-resolved cores and their density profiles are well fit by the pseudo-isothermal profile for radii well within the core radius r_c out to R_{200} . The isothermal profile fits the halo profiles near R_{200} to better than 20%, and even better further in. Best-fit values for the central core density vary between the haloes by a factor ~ 3 .

Fig. 4 shows the phase space density profiles of the nine P-WDM haloes represented in Fig. 3. The blue dashed lines show median values in radial bins of the six-dimensional coarse-grained phase space density profiles, F_{NB} , calculated using EnBiD. The horizontal red solid lines indicate the theoretically expected maximum fine-grained phase space density, $f_{\text{FD}}^{\text{max}}$, from Eqn. (2) for $mc^2 = 0.03$ keV, the WDM mass appropriate to the initial intrinsic velocities imparted to the particles in the simulations. Clearly, all the P-WDM haloes have an approximately flat phase space density profile near the centre. The maximum of this coarse-grained

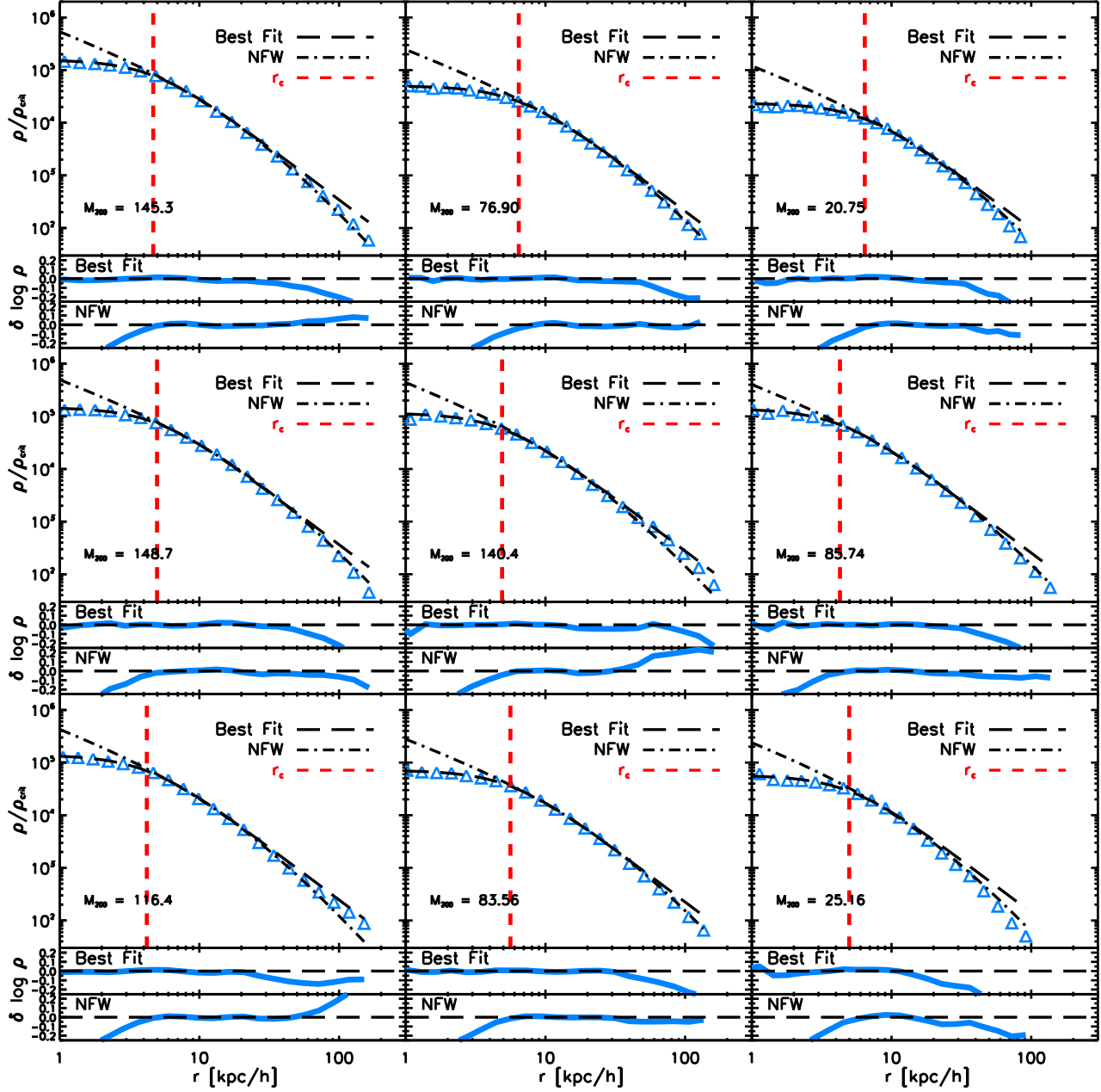


Figure 3. Spherically averaged density profiles of nine well-resolved haloes in our fiducial P-WDM simulations (blue triangles). The top three haloes are chosen from the higher-resolution P-WDM₅₁₂ simulation, while the rest are from the three P-WDM₂₅₆ simulations. The virial mass, M_{200} , in units of $10^{10} h^{-1} M_{\odot}$, is indicated in each panel. Fits using the pseudo-isothermal profiles of Eqn. (3) over the radial range $2\epsilon < r < r_{200}$ are shown by long dashed lines, with the best-fit core radius, r_c , indicated by vertical red lines. For comparison, the best fit NFW profile over the radial range $r_c < r < r_{200}$ is shown as the black dot-dashed line. The lower plots show the ratio of the measured densities to the best-fit NFW and pseudo-isothermal profiles. All nine haloes show a well-resolved core, and their profiles are well approximated by the pseudo-isothermal form from well inside r_c out to R_{200} .

density is very close to the fine-grained bound appropriate for the $mc^2 = 0.03$ keV WDM model.

The red horizontal dashed lines in Fig. 4 show $f_{\text{iso}}^{\text{max}}$, the maximum coarse-grained phase space density estimated from Eqn. (5) assuming a pseudo-isothermal profile and Maxwellian velocities. To calculate $f_{\text{iso}}^{\text{max}}$ we used the value of r_c which best fits the den-

sity profiles of Fig.3, and computed the one-dimensional velocity dispersion, σ , for all particles within r_c . For all nine haloes, the coarse-grained estimate, $f_{\text{iso}}^{\text{max}}$, is within 30 per cent of $f_{\text{FD}}^{\text{max}}$. Thus, it is possible to estimate $f_{\text{FD}}^{\text{max}}$ by measuring the core radius and velocity dispersion of the halo. If real galaxy haloes are dominated by WDM and baryons have little effect, then our simulations suggests

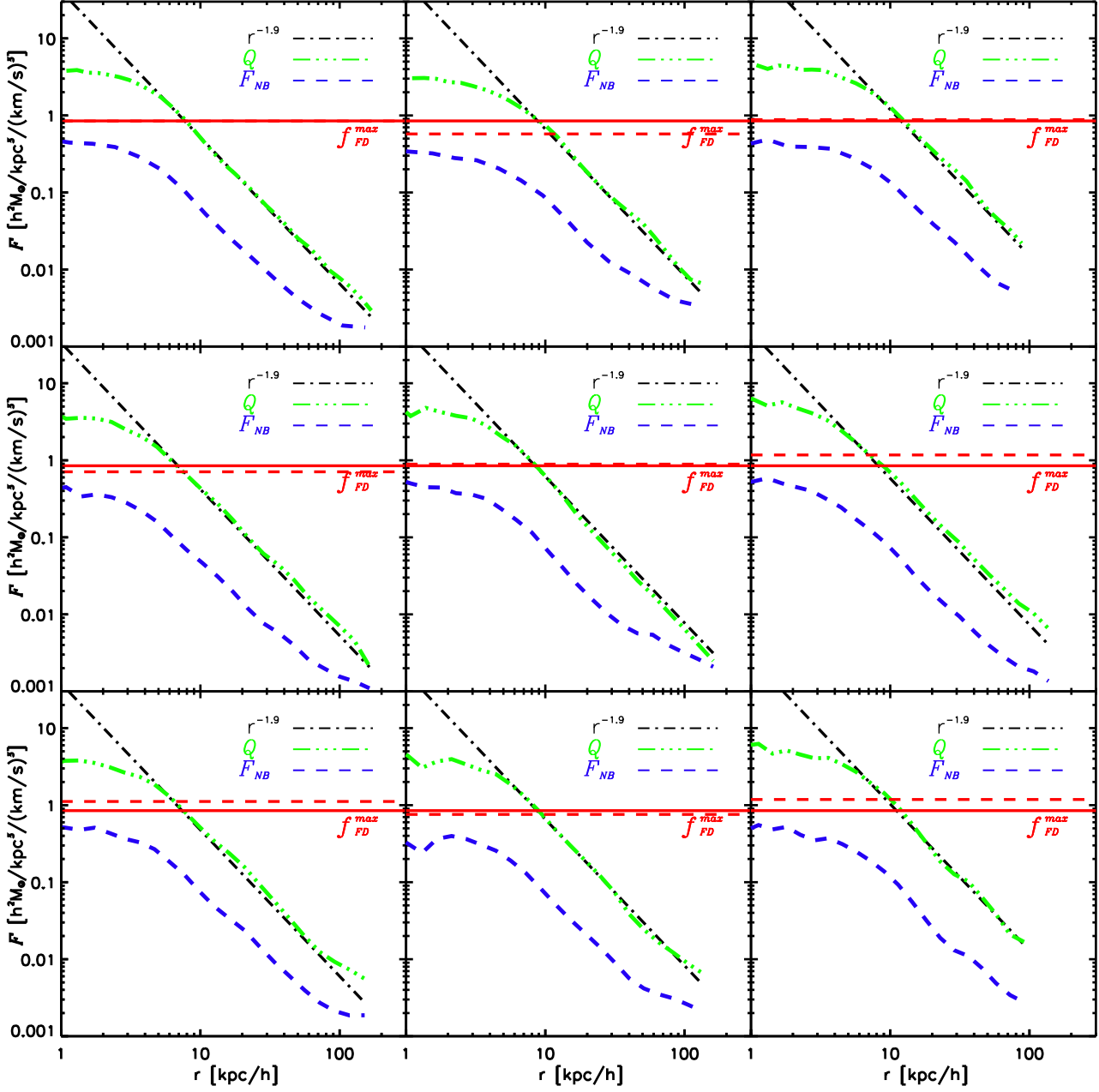


Figure 4. Spherically averaged coarse-grained phase space density profiles for the nine well-resolved haloes shown in Fig.3. The blue dashed lines show the median values in bins in radius, of the six-dimensional coarse-grained phase space density profiles, F_{NB} , calculated using EnBiD. The pseudo phase space density estimate, Q (Eqn.11), is shown in green, and a power law, $F \propto r^{-1.9}$ is shown in black. The red solid line indicates the upper limit to the fine-grained phase space density, $f_{\text{FD}}^{\text{max}}$, from Eqn. (2) for $mc^2 = 0.03$ keV, the value of m adopted in assigning WDM velocities in the simulations. The red dashed line indicates the upper limit $f_{\text{iso}}^{\text{max}}$ on F calculated from Eqn. (5) using the value of r_c that best fits the density profiles of Fig.3 and the velocity dispersion measured for the particles within r_c . These values are very close together. The maximum value reached by F_{NB} as computed using EnBiD (blue dashed line) is close to but smaller than the limits calculated by either the coarse-grained estimate $F_{\text{iso}}^{\text{max}}$ calculated from the halo's properties, or the fine-grained phase space limit, $f_{\text{FD}}^{\text{max}}$, appropriate for this P-WDM model. This demonstrates that the simulations satisfy Liouville's theorem, $F_{\text{NB}} < f_{\text{FD}}^{\text{max}}$, and that the WDM particle properties can be estimated from the halo profile, since $F_{\text{NB}}^{\text{max}} \lesssim F_{\text{iso}}^{\text{max}}$. In contrast, the pseudo phase space density, Q , overestimates F_{NB} by a factor of a few for some haloes, and up to an order of magnitude for others.

that it is possible to constrain the mass of a WDM particle, at least in principle. We apply this idea to dwarf galaxy data in the next section.

The pseudo phase space density, $Q \equiv \rho/\langle v^2 \rangle^{3/2}$, often used as a proxy for phase space density, is shown with green lines in Fig. 4. The shape of $Q(r)$ is similar to that of $F_{\text{NB}}(r)$, but its amplitude is offset to larger values by up to an order of magnitude. Clearly, using Q to estimate F_{NB} will result in incorrect constraints on WDM particle masses.

4 CONSTRAINING WDM PARTICLE MASSES FROM HALO PROFILES

We now apply the results of the previous section to the dwarf spheroidal satellites of the Milky Way. There are numerous claims in the literature that these galaxies have a central density core (e.g. Gilmore et al. 2007; Walker & Peñarrubia 2012, but see Strigari et al. (2010b)) and there have been attempts to interpret these using phase space density arguments, often with reference to WDM (e.g. Hogan & Dalcanton 2000; Dalcanton & Hogan 2001; Bode et al. 2001; Strigari et al. 2006; Simon & Geha 2007; Boyanovsky et al. 2008; Boyarsky et al. 2009a; de Vega & Sanchez 2010; Macciò et al. 2012). These studies usually assume that the stars in these galaxies are in dynamical equilibrium and closely trace the dark matter distribution in their parent dark matter haloes. Constraints on the mass of the WDM particle are then obtained by comparing the inferred phase space density with a theoretical expectation, often based on a proxy such as the pseudo phase space density, Q (e.g. Hogan & Dalcanton 2000); as we saw before this choice would lead to an incorrect result.

Our analysis shows that the maximum value of the coarse-grained phase space density in our N -body simulations is close both to the fundamental fine-grained bound, $f_{\text{FD}}^{\text{max}}$ (Eqn. 2), and to the estimate, $F_{\text{iso}}^{\text{max}}$ (Eqn. 5), calculated assuming a pseudo-isothermal profile and Maxwellian velocities. This result allows us to reassess previous constraints on WDM models and to set new rigorous limits on the WDM particle mass. In particular, we use the results from our simulations displayed in Fig. 4 that show that $F_{\text{iso}}^{\text{max}}$ differs from $f_{\text{FD}}^{\text{max}}$ by not more than about 30%. We proceed as follows.

We assume that the observed half-light radius of a dwarf spheroidal is approximately equal to the radius, R_h , at which the projected dark matter density attains half its central value. The projected surface density profile, $S(R)$, of the pseudo-isothermal model can be written as:

$$S(R) = \int_{-\infty}^{\infty} \rho[(R^2 + z^2)^{1/2}] dz = \frac{S_0 r_c}{\sqrt{r_c^2 + R^2}}, \quad (17)$$

where R is projected radius, and $S_0 = \pi \rho_0 r_c$ is the central surface density. Therefore $R_h = \sqrt{3} r_c$. We estimate the central one-dimensional velocity dispersion σ of the dark matter from the (measured) velocity dispersion of the stars within R_h . Combining these, we calculate the central maximum phase space density of the dark matter halo, $F_{\text{iso}}^{\text{max}}$, using Eqn. (5). Finally demanding that $F_{\text{iso}}^{\text{max}} \approx f_{\text{FD}}^{\text{max}}$, Eqn. (7), yields an estimate of the WDM particle mass, which we expect to be good to within 30 per cent. The inferred values are given in the last column of Table 2 and plotted in Fig. 5. Of course, these constraints are only relevant if the satellite dynamics are collisionless, so that Liouville's theorem is satisfied.

Our constraints on the maximum phase space density and $mc^2 g^{1/4}$ differ from other estimates in the literature based on dif-

ferent methods for estimating the maximum value of the coarse-grained phase space density. These estimates vary by factors of ~ 50 to ~ 0.2 for F , depending on the method used. For example, the limits from the model of Hogan & Dalcanton (2000) are a factor of 3.08 larger than ours. This disagreement is carried over to the limits set on $mc^2 g^{1/4}$ even when using the same data, by factors ranging from 0.65 to 2.75 (see also the illuminating summary and discussion in Boyarsky et al. (2009a)). In particular, our bounds on m are 1.54 times larger than those of Boyarsky et al. (2009a). Our method has the advantage over previous methods that it has been explicitly verified by N -body simulations.

The method outlined above yields an estimate of the mass of the WDM particle, $mc^2 (g/2)^{1/4} \approx 0.5$ keV, not a limit on m . This estimate is based on phase space considerations which, in turn, depend on the initial intrinsic velocities of the WDM particles. The lower limit inferred from the Lyman- α forest, $mc^2 \gtrsim 1.2$ keV, on the other hand, is determined by the cutoff in the power spectrum (Seljak et al. 2006; Viel et al. 2008; Boyarsky et al. 2009a). Although this cutoff is, of course, induced by free streaming due to the initial velocities, the two mass estimates exploit different properties of the initial WDM particle distribution, velocities in one case and the shape of the power spectrum in the other. For two of the satellites listed in Table 2 – Coma Berenices I and Canes Venatici II – the mass estimate from the phase space constraint and the lower limit from the Lyman- α forest are close. However, for the majority of the dwarf spheroidals in the table, the WDM particle mass inferred from the phase space constraint is significantly below the lower limit from the Lyman- α forest. For these objects the two methods can only be reconciled if the phase space density is lower than predicted by Liouville's theorem. This may result, for example, from energy exchange between the dark matter and the baryons in the halo.

5 SUMMARY AND DISCUSSION

Whether warm dark matter particles decouple as thermal relics or form from non-equilibrium decay, they acquire initial velocities whose amplitude depends on the particle's mass. Subsequent free streaming imposes a cut-off in the primordial spectrum of density perturbations. In this paper we have performed a series of numerical experiments to investigate how the intrinsic primordial velocity dispersion of fermionic dark matter particles affects the central density profile of the dark matter haloes into which they later collect. For WDM the initial velocities are small and resolving them in an N -body simulation of halo formation would require a currently prohibitively large number of simulation particles. Since we are primarily interested in the connection between the initial velocities and the final phase space distribution of the particles, we can circumvent this problem by decoupling the initial velocities from the free streaming length. Our simulations therefore do not correspond to a self-consistent representation of any particular WDM particle candidate but they are suitable for tackling the problem in hand. The power spectrum cut-off and primordial velocities we assumed correspond to those of thermally produced WDM particles of mass of 2 keV and 0.03 keV respectively. For comparison purposes, we also ran simulations of the standard Λ CDM case and a self-consistent WDM model with a particle mass of 2 keV.

Our main results may be summarised as follows:

- (i) Initial particle velocities induce cores in the radial profiles of both the physical and the phase space density of dark matter haloes.

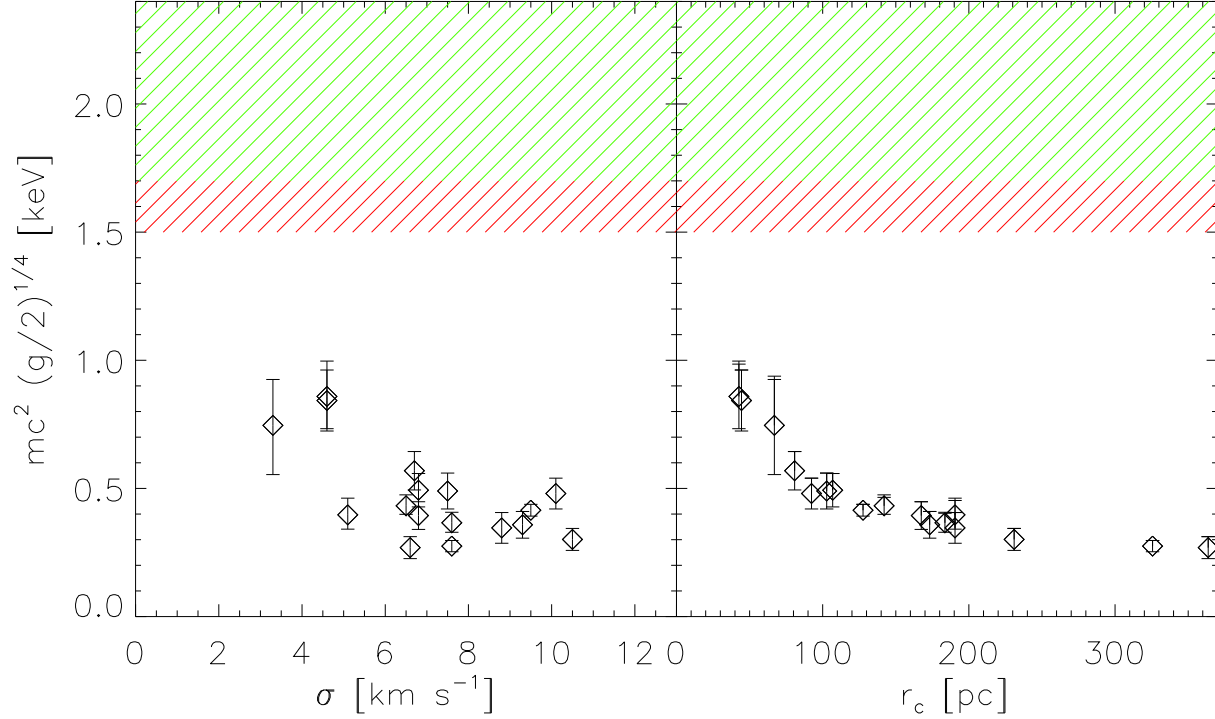


Figure 5. WDM particle mass, $mc^2 (g/2)^{1/4}$, inferred from the satellite properties of Table 2, as a function of the satellite velocity dispersion, σ (left), and core radius, r_c (right). For clarity, uncertainties on σ and r_c are not plotted. The value of m assumes that the coarse-grained phase space density, $F_{\text{iso}}^{\text{max}}$ (Eqn. 5), equals the theoretical bound, $f_{\text{FD}}^{\text{max}}$ (Eqn. 1). This analysis gives values of $mc^2 (g/2)^{1/4} \approx 0.5$ keV, approximately independently of σ or r_c . Hashed regions indicate the lower bound on m from the Lyman- α forest study of Boyarsky et al. (2009a), with their 99.7% and 95% confidence intervals (1.5 and 1.7 keV) shown in red and green respectively.

The inner density profile of the simulated haloes is well described by the pseudo-isothermal model (with a core).

(ii) The maximum coarse-grained phase space density of simulated haloes (computed using the EnBid code; Sharma & Steinmetz 2006) is very close to the theoretical fine-grained upper bound. This implies that it is, in principle, possible to use phase space arguments to constrain the nature of the dark matter.

(iii) In contrast, the pseudo phase space density, $Q \sim \rho/\sigma^3$, overestimates the maximum phase space density by a significant factor, up to an order of magnitude.

(iv) Assuming that the velocity distribution of the halo dark matter particles is Maxwellian, a simple analytical model that predicts the maximum allowed coarse-grained phase space density describes the simulations remarkably well (Fig. 3).

(v) Application of this analytic model to the kinematical data of dwarf spheroidal satellites of the Milky Way, assumed to have a pseudo-isothermal density profile with a core, constrains the mass of a hypothetical thermal fermionic WDM relic to be $mc^2 (g/2)^{1/4} \approx 0.5$ keV.

The low particle mass we infer from phase space considerations yields a large free-streaming mass, $M_{\text{FS}} \sim 10^{12} h^{-1} M_{\odot}$ (Eqn.16). As emphasized by Macciò et al. (2012), this is so large that a model with this kind of dark matter is unlikely to produce enough satellites in galaxies like the Milky Way. Whereas CDM may suffer from an excess of massive subhaloes – the ‘too big to

fail’ problem of Boylan-Kolchin et al. (2011), WDM may suffer from a ‘too small to succeed’ problem.

Our inferred value for m differs from other estimates in the literature based on different methods to estimate the coarse-grained phase space density, by factors ranging from 0.2 to 58. Our estimate, however, is the only one that has been explicitly validated using cosmological simulations of halo formation.

The inferred value of m follows from the assumption that the density profiles of the Milky Way dwarf spheroidal satellites have central cores. This assumption is controversial: for example Walker & Peñarrubia (2012) argue that cores are required by the data, at least for Fornax and Sculptor, but Strigari et al. (2010b) have shown explicitly that the data for these and other dwarfs are consistent with NFW cusps. In any case, the value of the particle mass required by the kinematical data, under the assumption that the dwarf spheroidal haloes do have cores, conflicts with the lower bound on the WDM particle mass set by observations of the Lyman- α forest which require the particles to have a mass $m \gtrsim 1.2$ keV (Seljak et al. 2006; Viel et al. 2008; Boyarsky et al. 2009a). This implies that if the cores are actually real, then they cannot be explained by the free-streaming velocities of thermally produced WDM particles. Instead, baryonic processes associated with the forming galaxy, for example, of the kind originally proposed by Navarro et al. (1996) and more recently seen in

dSph	R_h pc	σ km s ⁻¹	$F_{\text{iso}}^{\text{max}}$ $M_{\odot} \text{ kpc}^{-3} (\text{km s}^{-1})^{-3}$	$mc^2 (g/2)^{1/4}$ keV
dSphs from Gilmore et al. (2007)				
Sextans	630 ± 170	6.6 ± 2.3	$2.69^{+1.73}_{-1.73} \cdot 10^{-6}$	$0.269^{+0.043}_{-0.043}$
Fornax	400 ± 103	10.5 ± 2.7	$4.20^{+2.42}_{-2.42} \cdot 10^{-6}$	$0.301^{+0.043}_{-0.043}$
Leo I	330 ± 106	8.8 ± 2.4	$7.36^{+5.13}_{-5.13} \cdot 10^{-6}$	$0.346^{+0.060}_{-0.060}$
Ursa Minor	300 ± 74	9.3 ± 2.8	$8.42^{+4.87}_{-4.87} \cdot 10^{-6}$	$0.358^{+0.052}_{-0.052}$
Carina	290 ± 72	6.8 ± 1.6	$1.23^{+0.68}_{-0.68} \cdot 10^{-5}$	$0.394^{+0.054}_{-0.054}$
Draco	221 ± 16	9.5 ± 1.6	$1.52^{+0.34}_{-0.34} \cdot 10^{-5}$	$0.415^{+0.023}_{-0.023}$
Bootes	246 ± 28	$6.5^{+2.1}_{-1.3}$	$1.79^{+0.71}_{-0.54} \cdot 10^{-5}$	$0.432^{+0.043}_{-0.033}$
Sculptor	160 ± 40	10.1 ± 0.3	$2.73^{+1.37}_{-1.37} \cdot 10^{-5}$	$0.480^{+0.060}_{-0.060}$
Leo II	185 ± 48	6.8 ± 0.7	$3.03^{+1.60}_{-1.60} \cdot 10^{-5}$	$0.493^{+0.065}_{-0.065}$
dSphs from Simon & Geha (2007)				
Canes Venatici I	564 ± 36	7.6 ± 2.2	$2.92^{+0.92}_{-0.92} \cdot 10^{-6}$	$0.275^{+0.022}_{-0.022}$
Ursa Major I	318^{+50}_{-39}	7.6 ± 2.4	$9.17^{+4.09}_{-3.67} \cdot 10^{-6}$	$0.366^{+0.041}_{-0.037}$
Hercules	330^{+75}_{-52}	5.1 ± 2.4	$1.27^{+0.83}_{-0.72} \cdot 10^{-5}$	$0.397^{+0.065}_{-0.056}$
Leo T	178 ± 39	7.5 ± 2.7	$2.97^{+1.68}_{-1.68} \cdot 10^{-5}$	$0.490^{+0.070}_{-0.070}$
Ursa Major II	140 ± 25	6.7 ± 2.6	$5.37^{+2.83}_{-2.83} \cdot 10^{-5}$	$0.569^{+0.075}_{-0.075}$
Leo IV	116^{+26}_{-34}	3.3 ± 2.8	$1.59^{+1.52}_{-1.64} \cdot 10^{-4}$	$0.746^{+0.179}_{-0.192}$
Coma Berenices I	77 ± 10	4.6 ± 2.3	$2.58^{+1.46}_{-1.46} \cdot 10^{-4}$	$0.843^{+0.119}_{-0.119}$
Canes Venatici II	74^{+14}_{-10}	4.6 ± 2.4	$2.80^{+1.80}_{-1.64} \cdot 10^{-4}$	$0.859^{+0.138}_{-0.126}$

Table 2. Parameters for dwarf spheroidal satellites of the Milky Way: satellite name (col. 1); half-light radius and velocity dispersion compiled by Boyarsky et al. (2009a) (cols. 2 and 3); coarse-grained limit, $F_{\text{iso}}^{\text{max}}$, derived from the values of r_h and σ (col. 4); mass of the WDM particle assuming that the coarse-grained phase space, $F_{\text{iso}}^{\text{max}}$, equals the fine-grained value, $f_{\text{FD}}^{\text{max}}$ (col. 5).

simulations (e.g. Read & Gilmore 2005; Mashchenko et al. 2008; Governato et al. 2010; Brooks & Zolotov 2012) would be required.

ACKNOWLEDGEMENTS

It is a pleasure to thank Simon D. M. White, Adrian Jenkins, Alexey Boyarsky, Oleg Ruchayskiy & Andrea Macció, for helpful discussions. Some of simulations used in this work were carried out on the Lenova Deepcomp7000 supercomputer of the super Computing Centre of Chinese Academy of Sciences, Beijing, China. LG acknowledges support from the one-hundred-talents program of the Chinese academy of science (CAS), the National Basic Research Program of China (program 973 under grant No. 2009CB24901), NSFC grants (Nos. 10973018 and 11133003), MPG partner Group family, and an STFC Advanced Fellowship, as well as the hospitality of the Institute for Computational Cosmology at Durham University. CSF acknowledges a Royal Society Wolfson Research Merit Award and ERC Advanced Investigator grant COSMIWAY. This work was supported in part by an STFC rolling grant to the ICC.

REFERENCES

- Arad I., Dekel A., Klypin A., 2004, MNRAS, 353, 15
- Ascasibar Y., Binney J., 2005, MNRAS, 356, 872
- Ascasibar Y., Yepes G., Gottlöber S., Müller V., 2004, MNRAS, 352, 1109
- Begeman K. G., Broeils A. H., Sanders R. H., 1991, MNRAS, 249, 523
- Bode P., Ostriker J. P., Turok N., 2001, ApJ, 556, 93
- Bond J. R., Szalay A. S., 1983, ApJ, 274, 443
- Boyanovsky D., de Vega H. J., Sanchez N. G., 2008, Phys Rev D, 77, 4, 043518
- Boyarsky A., Ruchayskiy O., Iakubovskiy D., 2009a, JCAP, 3, 5
- Boyarsky A., Ruchayskiy O., Shaposhnikov M., 2009b, Annual Review of Nuclear and Particle Science, 59, 191
- Boylan-Kolchin M., Bullock J. S., Kaplinghat M., 2011, MNRAS, 415, L40
- Brooks A. M., Zolotov A., 2012, ArXiv e-prints
- Cole S., Percival W. J., Peacock J. A., et al., 2005, MNRAS, 362, 505
- Colín P., Valenzuela O., Avila-Reese V., 2008, ApJ, 673, 203
- Colless M., Jones H., Campbell L., Burkey D., Taylor A., Saunders W., 2005, in Maps of the Cosmos, edited by M. Colless, L. Staveley-Smith, R. A. Stathakis, vol. 216 of IAU Symposium,

- 180
- Dalcanton J. J., Hogan C. J., 2001, *ApJ*, 561, 35
- de Vega H. J., Sanchez N. G., 2010, *MNRAS*, 404, 885
- Dehnen W., McLaughlin D. E., 2005, *MNRAS*, 363, 1057
- Diemand J., Kuhlen M., Madau P., et al., 2008, *Nature*, 454, 735
- Feng J. L., 2010, *ARA&A*, 48, 495
- Frenk C. S., White S., 2012, *Annalen der Physik*, in press
- Frenk C. S., White S. D. M., Davis M., 1983, *ApJ*, 271, 417
- Gao L., Navarro J. F., Frenk C. S., Jenkins A., Springel V., White S. D. M., 2012, *ArXiv e-prints*
- Gao L., Theuns T., 2007, *Science*, 317, 1527
- Gilmore G., Wilkinson M. I., Wyse R. F. G., et al., 2007, *ApJ*, 663, 948
- Governato F., Brook C., Mayer L., et al., 2010, *Nature*, 463, 203
- Green A. M., Hofmann S., Schwarz D. J., 2005, *JCAP*, 8, 3
- Hoffman Y., Romano-Díaz E., Shlosman I., Heller C., 2007, *ApJ*, 671, 1108
- Hogan C. J., Dalcanton J. J., 2000, *Phys Rev D*, 62, 6, 063511
- Hooper D., 2012, *ArXiv e-prints*
- Kent S. M., 1986, *AJ*, 91, 1301
- Kolb E. W., Turner M. S., 1990, *The early universe*.
- Komatsu E., Smith K. M., Dunkley J., et al., 2011, *ApJS*, 192, 18
- Lovell M. R., Eke V., Frenk C. S., et al., 2012, *MNRAS*, 420, 2318
- Lynden-Bell D., 1967, *MNRAS*, 136, 101
- Macciò A. V., Paduroiu S., Anderhalden D., Schneider A., Moore B., 2012, *MNRAS*, 424, 1105
- Madsen J., 1991, *Phys Rev D*, 44, 999
- Mashchenko S., Wadsley J., Couchman H. M. P., 2008, *Science*, 319, 174
- Mathur S. D., 1988, *MNRAS*, 231, 367
- Navarro J. F., Frenk C. S., White S. D. M., 1996, *ApJ*, 462, 563
- Navarro J. F., Frenk C. S., White S. D. M., 1997, *ApJ*, 490, 493
- Navarro J. F., Ludlow A., Springel V., et al., 2010, *MNRAS*, 402, 21
- Parry O. H., Eke V. R., Frenk C. S., Okamoto T., 2012, *MNRAS*, 419, 3304
- Peebles P. J. E., Yu J. T., 1970, *ApJ*, 162, 815
- Peirani S., Durier F., de Freitas Pacheco J. A., 2006, *MNRAS*, 367, 1011
- Pontzen A., Governato F., 2012, *MNRAS*, 421, 3464
- Pryor C., Kormendy J., 1990, *AJ*, 100, 127
- Read J. I., Gilmore G., 2005, *MNRAS*, 356, 107
- Seljak U., Makarov A., McDonald P., et al., 2005, *Phys Rev D*, 71, 10, 103515
- Seljak U., Slosar A., McDonald P., 2006, *JCAP*, 10, 14
- Seljak U., Zaldarriaga M., 1996, *ApJ*, 469, 437
- Sharma S., Steinmetz M., 2006, *MNRAS*, 373, 1293
- Simon J. D., Geha M., 2007, *ApJ*, 670, 313
- Springel V., 2005, *MNRAS*, 364, 1105
- Springel V., Wang J., Vogelsberger M., et al., 2008, *MNRAS*, 391, 1685
- Stadel J., Potter D., Moore B., et al., 2009, *MNRAS*, 398, L21
- Strigari L. E., Bullock J. S., Kaplinghat M., et al., 2006, *ApJ*, 652, 306
- Strigari L. E., Frenk C. S., White S. D. M., 2010a, *MNRAS*, 408, 2364
- Strigari L. E., Frenk C. S., White S. D. M., 2010b, *MNRAS*, 408, 2364
- Taylor J. E., Navarro J. F., 2001, *ApJ*, 563, 483
- Tremaine S., Gunn J. E., 1979, *Physical Review Letters*, 42, 407
- Tremaine S., Henon M., Lynden-Bell D., 1986, *MNRAS*, 219, 285
- Vass I. M., Valluri M., Kravtsov A. V., Kazantzidis S., 2009, *MNRAS*, 395, 1225
- Viel M., Becker G. D., Bolton J. S., Haehnelt M. G., Rauch M., Sargent W. L. W., 2008, *Physical Review Letters*, 100, 4, 041304
- Viel M., Haehnelt M. G., Springel V., 2010, *JCAP*, 6, 15
- Vogelsberger M., Helmi A., Springel V., et al., 2009, *MNRAS*, 395, 797
- Vogelsberger M., White S. D. M., Helmi A., Springel V., 2008, *MNRAS*, 385, 236
- Walker M., Peñarrubia J., 2012, in *Dynamics Meets Kinematic Tracers*
- Wang J., Frenk C. S., Cooper A. P., 2012, *ArXiv e-prints*
- Zehavi I., Zheng Z., Weinberg D. H., et al., 2011, *ApJ*, 736, 59
- Zel'dovich Y. B., 1965, *Adv. Astron. Astrophys.*